# Effect of Eu$^{3+}$ on the Structural, Magnetic and Mössbauer Spectroscopy Studies of Copper Ferrite

V. Jagadeesha Angadi [a,*], I.S. Yahia [b,c,d], H.Y. Zahran [b,c,d], M.C. Oliveira [e], E. Longo [e],
S.P. Kubrin [f], S.O. Manjunatha [g], R.A.P. Ribeiro [h,*], M.H. Ghozza [i]

[a] Department of Physics, P.C. Jabin Science College, Hubballi 580031, India
[b] Laboratory of Nano-Smart Materials for Science and Technology (LNSMST), Department of Physics, Faculty of Science, King Khalid University, P.O. Box 9004, Abha, Saudi Arabia
[c] Research Center for Advanced Materials Science (RCAMS), King Khalid University, P.O. Box 9004, Abha 61413, Saudi Arabia
[d] Nanoscience Laboratory for Environmental and Biomedical Applications (NLEBA), Semiconductor Lab., Metallurgical Lab. 1, Department of Physics, Faculty of Education, Ain Shams University, Roxy, Cairo 11757, Egypt
[e] Center for the Development of Functional Materials (CDMF), Federal University of São Carlos, São Carlos, SP, Brazil
[f] Research Institute of Physics, Southern Federal University, Rostov-on-Don 344090, Russia
[g] Department of Physics, B.M.S College of Engineering, Bengaluru 560019, India
[h] Department of Chemistry, Minas Gerais State University, Divinópolis, MG, Brazil
[i] Basic Science Deparment, Marg High Institute of Engineering and Modern Technology, Cairo, Egypt

## ARTICLE INFO

## ABSTRACT

Here, theoretical and practical methods were used to study the impact of Eu$^{3+}$ substitution on copper ferrites. The spinel cubic structure of the synthesised samples is crystalline, and XRD analysis revealed the presence of a trace amount of the impurity Fe$_2$O$_3$ phase. The range of the estimated crystallite sizes is between 18 and 27 nm. FTIR spectra of the ferrites exhibited the presence of functional groups of spinel ferrites. The temperature-dependent Mössbauer spectra of CuFe$_{2-x}$Eu$_x$O$_4$ (x = 0, 0.01, 0.02, 0.03) (CEF) were collected at 300 K, 200 K, 100 K, and 14 K. Room temperature spectra consist of asymmetrically broadened sextets and quadruple split lines. The intensity of quadrupole split lines decreases along with the reduction in temperature. The observed changes in the structure of the Mössbauer spectra are typical of nanosized particles. The presence of paramagnetic lines at temperatures lower than the Curie temperature, asymmetric lines with sharp external fronts, and significantly diffused internal fronts is a sign of superparamagnetic relaxation. The partial substitution of Fe$^{3+}$ ions by Eu$^{3+}$ ions causes the redistribution of A and B cations, which leads to the alteration in angle and bond length of magnetic superexchange links. DFT calculations support the preference for octahedral Eu-doping in combination with the CuFe$_2$O$_4$ matrix, which results in local structural disorders that affect both the material's magnetic and electrical characteristics. The size, shape, interaction with the matrix, and crystallite characteristics all affect the material's magnetic properties. A weak ferromagnetic characteristic is indicated by the magnetic properties, and the magnetization values increase as Eu increases as a result of changes in crystallite size. As a result, our findings imply that synthesised samples are appropriate for applications involving hyperthermia.

## 1. Introduction

Copper ferrites (CuFe$_2$O$_4$) are a one-of-a-kind soft magnetic material that has piqued the interest of researchers due to their low electrical resistivity, high permeability, chemical stability, cost-effectiveness, and mechanical hardness [1–5]. The structural, electrical, microstructural, spectroscopic, magnetic, and absorption properties of CuFe$_2$O$_4$ ferrites are now being actively researched [1,6–8]. However, these features of CuFe$_2$O$_4$ ferrites can be improved by doping rare-earth ions (Pr$^{3+}$, Gd$^{3+}$, Yb$^{3+}$, Nd$^{3+}$, Sm$^{3+}$, La$^{3+}$, and so on) in the ferrite matrix [9–16]. Because rare-earth ions have unpaired 4f electrons with strong spin-orbit coupling, a modest amount of rare-earth ions that replaced Fe$^{3+}$ sites in ferrites has demonstrated a substantial increase in electrical and magnetic properties. The substitution of rare-earth ions at the Fe$^{3+}$ site
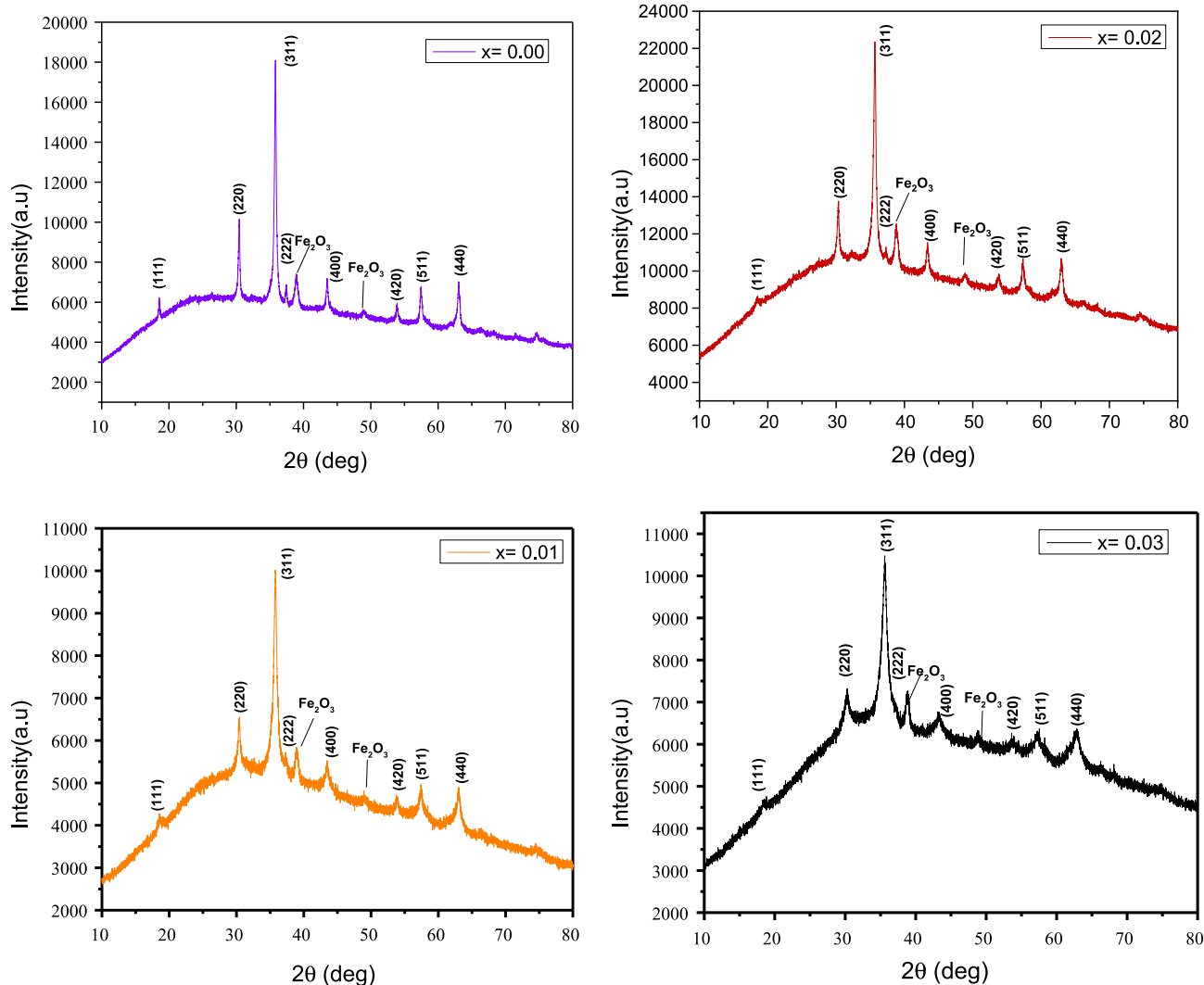
**Fig. 1.** XRD pattern of $CuFe_{(2-x)}Eu_xO_4$ (where, x = 0.00 0.01, 0.02 and 0.03).

**Table 1**

Structural parameters of the $CuFe_{(2-x)}Eu_xO_4$ (where, x = 0.00 0.01, 0.02 and 0.03) nanoparticles.

| $Eu^{3+}$ content | Crystallite Size D in (nm) | Lattice parameters (Å) | Strain Є (radian) | Volume (Å$^3$) | Hoping length (Å) | |
|---|---|---|---|---|---|---|
| | | | | | $L_A$ | $L_B$ |
| x = 0.0 | 25 | 8.126 | $1.38 \times 10^{-3}$ | 539.29 | 3.518 | 2.873 |
| x = 0.01 | 16 | 8.131 | $2.14 \times 10^{-3}$ | 540.23 | 3.520 | 2.874 |
| x = 0.02 | 21 | 8.143 | $1.63 \times 10^{-3}$ | 542.71 | 3.526 | 2.879 |
| x = 0.03 | 51 | 8.154 | $6.98 \times 10^{-3}$ | 544.91 | 3.531 | 2.883 |

causes 4f-3d coupling, which aids in determining the magneto-crystalline anisotropy of the material [17–19]. Rare-earth doping is essential for ferrite nucleation and development, as it favors magnetic spin orientation for the desired magnetic characteristics [17,18,20]. The interaction of Fe–Fe is known to regulate the magnetic behavior of spinel ferrite compounds. Rare-earth ions penetrate the spinel lattice's octahedral site, causing 4f-3d interactions that cause structural distortion, lattice strain, and saturation magnetization shifts [21–23]. As a result, the various properties of rare-earth ions may effectively modulate the
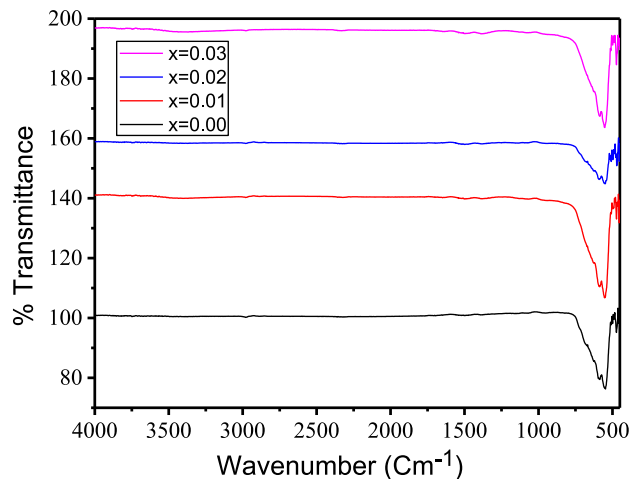


**Fig. 2.** FTIR spectra of $CuFe_{(2-x)}Eu_xO_4$ (where, x = 0.00 0.01, 0.02 and 0.03).

dielectric and magnetic properties of $CuFe_2O_4$ spinel nano ferrites. Further ferrites are principally utilized as multilayer chip inductors (MLCI) in electronics as well as inductors, transformer cores, deflection yokes, and recording heads. Further spinel ferrites also used for high-
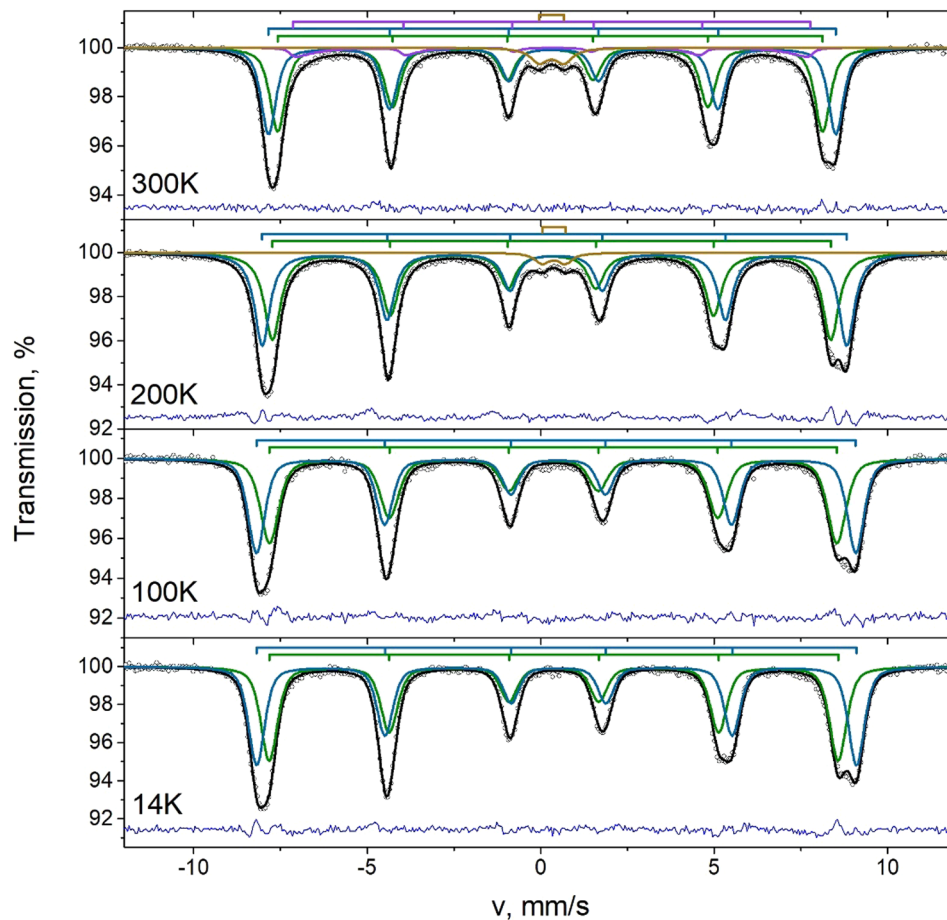
**Fig. 3.** Mössbauer spectra of CuFe$_2$O$_4$ nanoparticles taken at different temperatures. (Greed line – S$_A$ sextet, Light blue line – S$_B$ sextet, Viol line – relaxation sestet, Dark yellow line – Doublet for unblocked particles).

frequency and permanent magnet applications [56,57,58,59,60].

Spinel ferrites can be made using a variety of techniques, including sol-gel auto combustion, co-precipitation, sonochemical processes, mechanical alloying, solution combustion method, and hydrothermal procedures [24–26]. Herein, the self-propagating high-temperature synthesis approach was employed in this study to prepare pure (CuFe$_2$O$_4$) and rare-earth-doped (Eu) copper nanoferrites (CuFe$_{2-x}$Eu$_x$O$_4$). The role of Eu doping on vibrational, magnetic, structural, and low-temperature Mössbauer studies of copper nanoferrites was explored using various characterization techniques to determine their suitability in magnetic devices.

## 2. Methods

### 2.1. Synthesis

CuEu$_x$Fe$_{2-x}$O$_4$ NPs were synthesized by using a stoichiometry quantity of fuels and metal nitrates and urea [NH$_2$CONH$_2$] and glucose [C$_6$H$_{12}$O$_6$] as fuels. Considering the complete combustion reaction, the mixture of both fuels were taken, such that, the oxidizer to fuel ratio to be unity using the oxidizing the reducing valencies of metal nitrates and fuels. The stoichiometric amounts of the metal nitrates and fuels were dissolved with 30 ml double distilled water and thoroughly stirred on the magnetic stirrer at a static spinning speed of 800 rpm for 1 h until clear transparent solution. This clear transparent solution is called redox mixture. The redox mixture was then taken in a 250 ml borosil beaker and kept in a pre-heated muffle furnace at 450 °C. Initially, the solution boils then froths and ignites to yield fine ash. The final as was then ground in agate pestle mortar and collected. To mention, the whole

combustion process has gets completed in less than 20 min, whereas the reaction time of the actual ignition/flaming was few seconds.

#### 2.1.1. Characterization

XRD was used to characterize the fine powder samples to understand the crystalline structure and phase. XRD was performed using CuK$_\alpha$ radiation, and the diffractogram data was recorded from 10° to 80° with a step size of 0.02°. The FTIR spectra were recorded to confirm the samples' vibrational bands using an IRTracer-100 Shimadzu FTIR spectrometer.

The fine powder samples were characterized using XRD to determine the crystalline structure and phase. CuK$_\alpha$ radiation was used for XRD, and the diffractogram data was recorded with a step size of 0.02° from 10° to 80°. An IRTracer-100 Shimadzu FTIR spectrometer was used to record the FTIR spectra in order to confirm the vibrational bands of the samples. The MS1104Em spectrometer was used to record the Mössbauer spectra. Southern Federal University's Scientific Research Institute of Physics planned and built it. The geometry of a moving source is used. 57Co in a rhodium matrix was used as the source of -quanta. As a function of the metallic α-Fe, the isomer shifts were determined. In a CCS-850 helium cryostat chamber, the samples were chilled. The SpectrRelax software was used to fit the spectra. The samples are investigated using a PPMS-14 T vibrating sample magnetometer to determine the magnetic properties and magnetic nature of the samples.

### 2.2. Theoretical details

In this study, the Eu-doped copper nanoferrites were investigated

**Table 2**

Mössbauer parameters of $CuFe_{2-x}Eu_xO_4$ nanoparticles. In this case, δ – isomer shift, ε – quadrupole shift, Δ – quadrupole splitting for paramagnetic component, H – hyperfine magnetic field on $^{57}Fe$ nucleus, Γ – linewidth, A – component area.

| x | T, K | Component | δ ± 0.01, mm/s | ε/Δ ± 0.01, mm/s | H ± 0.4, kOe | A ± 0.5, % | Γ ± 0.01, mm/s |
|---|---|---|---|---|---|---|---|
| 0 | 300 | D1 | 0.33 | 0.72 | | 4.5 | 0.60 |
| | | S1 | 0.27 | 0.00 | 487.0 | 44.5 | 0.54 |
| | | S2 | 0.36 | −0.02 | 507.1 | 44.5 | 0.52 |
| | | SR | 0.32 | −0.02 | 462.2 | 6.5 | 0.29 |
| | 200 | D1 | 0.38 | 0.60 | | 2.5 | 0.51 |
| | | S1 | 0.32 | 0.00 | 499.1 | 48.8 | 0.57 |
| | | S2 | 0.42 | −0.03 | 522.4 | 48.8 | 0.53 |
| | 100 | S1 | 0.37 | −0.01 | 507.0 | 50.0 | 0.64 |
| | | S2 | 0.47 | −0.03 | 535.6 | 50.0 | 0.57 |
| | 14 | S1 | 0.38 | 0.00 | 508.5 | 50.0 | 0.58 |
| | | S2 | 0.49 | 0.00 | 536.1 | 50.0 | 0.55 |
| 0.01 | 300 | D1 | 0.35 | 0.72 | | 28.8 | 0.58 |
| | | S1 | 0.29 | −0.01 | 477.3 | 26.9 | 0.50 |
| | | S2 | 0.34 | −0.02 | 499.7 | 31.3 | 0.52 |
| | | SR | 0.31 | −0.03 | 471.3 | 22.3 | 0.29 |
| | 200 | D1 | 0.43 | 0.72 | 0.0 | 11.4 | 0.51 |
| | | S1 | 0.34 | 0.00 | 500.9 | 32.5 | 0.55 |
| | | S2 | 0.43 | −0.03 | 532.1 | 30.7 | 0.53 |
| | | SR | 0.35 | −0.03 | 488.7 | 25.4 | 0.29 |
| | 100 | D1 | 0.49 | 0.64 | 0.0 | 5.8 | 0.36 |
| | | S1 | 0.38 | 0.00 | 506.5 | 39.9 | 0.56 |
| | | S2 | 0.48 | −0.02 | 532.1 | 38.1 | 0.54 |
| | | SR | 0.39 | −0.04 | 495.4 | 16.2 | 0.29 |
| | 14 | S1 | 0.39 | 0.01 | 507.5 | 44.4 | 0.53 |
| | | S2 | 0.48 | −0.02 | 533.0 | 42.6 | 0.54 |
| | | SR | 0.39 | −0.03 | 495.3 | 13 | 0.29 |
| 0.02 | 300 | D1 | 0.33 | 0.76 | | 18.1 | 0.55 |
| | | S1 | 0.29 | 0.00 | 482.3 | 31.1 | 0.62 |
| | | S2 | 0.34 | 0.00 | 501.9 | 27.5 | 0.48 |
| | | SR | 0.32 | 0.01 | 473.1 | 23.3 | 0.29 |
| | 200 | D1 | 0.40 | 0.81 | | 15.8 | 0.67 |
| | | S1 | 0.34 | −0.01 | 501.3 | 35.7 | 0.60 |
| | | S2 | 0.42 | −0.01 | 523.4 | 32.1 | 0.50 |
| | | SR | 0.37 | 0.00 | 480.0 | 16.4 | 0.29 |
| | 100 | D1 | 0.47 | 0.84 | | 3.9 | 0.70 |
| | | S1 | 0.39 | 0.00 | 507.9 | 44.4 | 0.60 |
| | | S2 | 0.47 | 0.00 | 532.2 | 40.6 | 0.52 |
| | | SR | 0.40 | −0.01 | 483.0 | 11.1 | 0.29 |
| | 14 | S1 | 0.40 | 0.00 | 507.5 | 46.3 | 0.55 |
| | | S2 | 0.48 | 0.00 | 532.5 | 42.9 | 0.52 |
| | | SR | 0.41 | 0.00 | 485.9 | 10.7 | 0.29 |
| 0.03 | 300 | D1 | 0.33 | 0.74 | | 30.5 | 0.66 |
| | | S1 | 0.29 | 0.00 | 471.8 | 16.7 | 0.62 |
| | | S2 | 0.37 | −0.03 | 499.1 | 11.0 | 0.51 |
| | | SR | 0.31 | −0.01 | 462.8 | 41.8 | 0.29 |
| | 200 | D1 | 0.40 | 0.78 | | 12.9 | 0.66 |
| | | S1 | 0.34 | 0.00 | 484.8 | 26.7 | 0.62 |
| | | S2 | 0.41 | −0.02 | 513.3 | 21.2 | 0.59 |
| | | SR | 0.36 | −0.01 | 468.5 | 39.1 | 0.29 |
| | 100 | D1 | 0.45 | 0.74 | | 3.6 | 0.59 |
| | | S1 | 0.40 | 0.00 | 494.3 | 43.4 | 0.61 |
| | | S2 | 0.47 | −0.01 | 525.3 | 38.1 | 0.64 |
| | | SR | 0.43 | 0.00 | 470.0 | 14.8 | 0.29 |
| | 14 | S1 | 0.40 | 0.00 | 501.6 | 46.4 | 0.55 |
| | | S2 | 0.49 | −0.01 | 531.5 | 41.0 | 0.59 |
| | | SR | 0.44 | −0.02 | 478.6 | 12.5 | 0.29 |

using density functional theory with PBE0 [27] hybrid functional implemented in the CRYSTAL17 [28] package. First, the cubic unit cell for $CuFe_2O_4$ was minimized as a function of the system's total energy. Three magnetic models (FEM, FiM-I and FiM-II) were used to investigate the magnetic properties. [29] Based on the primitive (14 atoms) unit cell of inverse $CuFe_2O_4$, the six magnetic sites can be described as ($Fe_{Tetra}$, $Fe_{Tetra}$, $Cu_{Octa}$, $Cu_{Octa}$, $Fe_{Octa}$, $Fe_{Octa}$), where FEM (↑↑↑↑↑↑), FiM-I (↑↑↓↓↓↓) and FiM-II (↑↑↑↑↓↓).

The Eu-doped copper ferrites model was based on the conventional supercell (56 atoms), and $Eu^{3+}$ successively replaced the $Fe^{3+}$ atoms. In order to analyze the preferential site for Eu doping, both tetrahedral and octahedral $Fe^{3+}$ were considered. Cu, Fe were represented by all-electron 86-411d41G [30,31], Eu by effective core pseudopotential including valence 4f orbital representation [32], and 8411d1 Gaussian basis sets were used to represent the O atoms [33]. The optimization criteria was set as $10^{-8}$ Hartree, and the accuracy of the Coulomb and exchange series was controlled by two sets of parameters defined as $10^{-8}$ and $10^{-16}$. The k-points were defined by a shrinking factor set to $8 \times 8$ (Gillat Web), following the Monkhorst–Pack method [34].

## 3. Results and discussions

### 3.1. Structural analysis

*Fd-3 m* space group polycrystalline spinel cubic structure with modest $Fe_2O_3$ impurity phase was observed in all samples [35,36]. In hyperfine interaction investigations, this impurity will have no effect. The indexed XRD (Fig. 1) peaks follow JCPDS card number 74-2400. Due to the difference in ionic radius, the lattice parameter increases with increasing $Eu^{3+}$ concentration. It has been confirmed that europium occupies an octahedral position due to the smaller ionic radius of $Fe^{3+}$ (0.67). All samples were found to have an average particle size in the range of 16–51 nm, as determined by the Debye-Scherrer relation and the average crystallite size inferred from the Debye-Scherrer relationship [37,38]. We previously reported values for crystallite size, lattice parameter, and other essential characteristics (see Table 1).

### 3.2. Vibrational analysis

Infrared spectra have been used to examine ion positions in crystals and vibrational modes. CEF FTIR spectra are shown in Fig. 2. The band at 472 $cm^{-1}$ was given to octahedral complexes in the FTIR spectra of all the samples, while 548 $cm^{-1}$ was ascribed to tetrahedral complexes [39,40]. Because of the absence of shoulders in the first absorption band, the potential of $Fe^{2+}$ ions at A-sites has been ruled out. On the other hand, the octahedral complexes are a result of a simple splitting of the absorption band at 472 $cm^{-1}$ [41,42]. Iron and rare-earth ions on B-sites in oxide state are thought to be responsible for this Jahn Teller distortion, as confirmed by XRD. The absorption bands differ due to variations in bond lengths at tetrahedral and octahedral sites, respectively. There is a slight variance in-band location owing to the preparation technique, grain size, and porosity. With increasing the doping amount, there may be a change in the spectrum due to the increased quantity of rare earth in materials.

### 3.3. Mössbauer analysis

The Mössbauer spectra of $CuFe_{2-x}Eu_xO_4$ (x = 0, 0.01, 0.02, 0.03) were collected at 300 K, 200 K, 100 K and 14 K. Room temperature spectra (Fig. 3) consist of asymmetrically broadened sextets and quadruple split lines. The reduction in temperature leads to an increase in the line intensity of sextets and a narrowing of resonant lines. Furthermore, the intensity of quadrupole split lines decreases along with temperature reduction. The observed changes in the structure of Mössbauer spectra are typical of nanosized particles. The presence of paramagnetic lines at temperatures lower than the Curie temperature and asymmetric lines with sharp external fronts and significantly diffused internal fronts is the sin of superparamagnetic relaxation [43,44]. The magnetic sextets relate to nanoparticles with a blocked magnetic moment, while quadrupole lines correspond to unblocked particles. The unblocked particles have a very high rate of magnetic moments rotation, which leads to a collapse of Zeeman splitting. According to scanning electron microscope study results, the $CuFe_{2-x}Eu_xO_4$ (x = 0, 0.01, 0.02, 0.03) nanoparticles are characterized by a wide distribution of grain sizes [4]. The grain sizes in this system vary between 0 and 60 nm. The critical size for $CuFe_2O_4$ is about 7 nm [45,46].
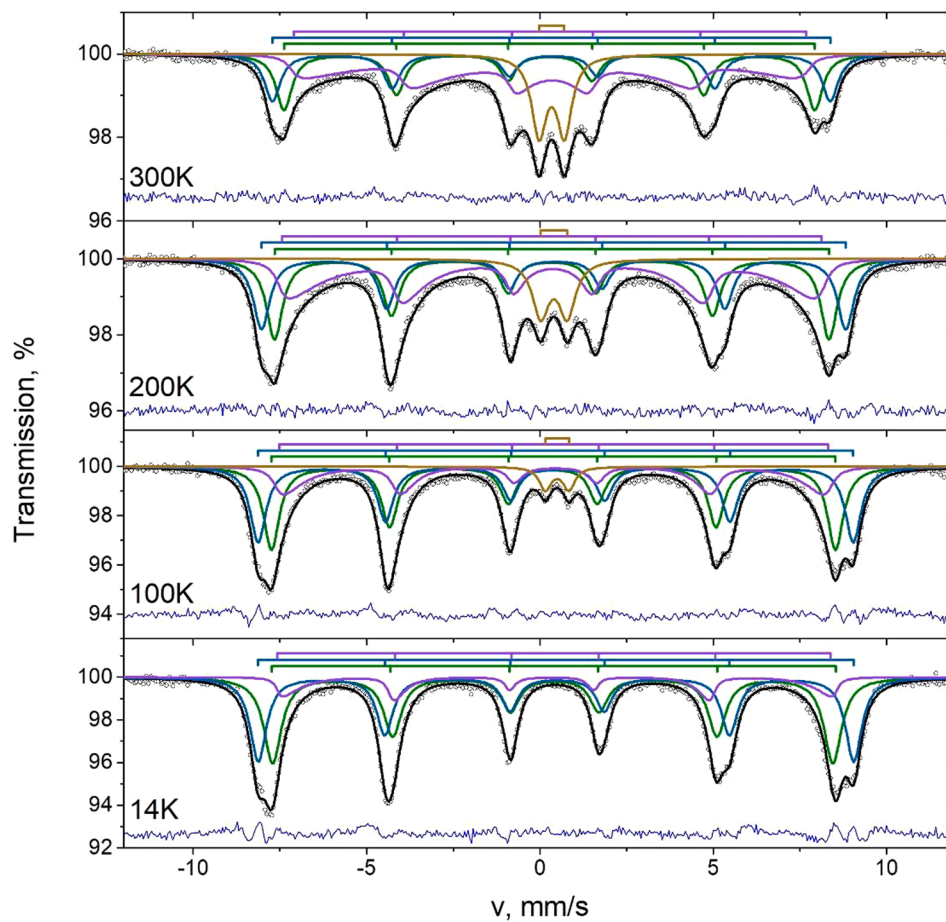
**Fig. 4.** Mössbauer spectra of $CuFe_{2-x}Eu_xO_4$ (x = 0.1) nanoparticles taken at different temperatures. (Greed line – $S_A$ sextet, Light blue line – $S_B$ sextet, Viol line – relaxation sestet, Dark yellow line – Doublet for unblocked particles).

Therefore, the magnetic sextets are associated with nanoparticles, with the grain size being larger than 10 nm. The quadrupole lines correspond to nanoparticles with diameters lower than 10 nm. Since the samples have a wide distribution of grain sizes, there are particles with a relaxation time close to Mössbauer measurement time ($\tau_m = 2.5 \bullet 10^{-8}$ s). The presence of such particles leads to the appearance of a relaxation component in the Mössbauer spectra. Thus, the Mössbauer spectra of $CuFe_{2-x}Eu_xO_4$ (x = 0, 0.01, 0.02, 0.03) decompose into magnetic sextets, doublets and relaxation components. In order to describe the relaxation process, the many-state superparamagnetic relaxation (MSSR) model [47] was used for the fitting.

The room temperature spectra of $CuFe_{2-x}Eu_xO_4$ (x = 0, 0.01, 0.02, 0.03) samples (Fig. 3) consist of two sextets ($S_A$ and $S_B$), a paramagnetic doublet (D) and a MSSR sextet (SR). The parameters of these subspectra are listed in Table 2. The isomer shift of all subspectra corresponds to the $Fe^{3+}$ ions. The isomer shift values of $S_A$ and $S_B$ sextets are typical of $Fe^{3+}$ in tetrahedron and octahedron, respectively [54,55]. The area value of the doublet increased from 4.5% to 30.5% with x growing, indicating that the fractions of nanoparticles with a grain size lower than 10 nm increased along with the growth of $Eu^{3+}$ concentration. The area of the doublet decreases as a result of temperature reduction (Figs. 4, 5, 6), meaning that the fraction of unblocked nanoparticles decreases due to blocking magnetic moments of particles of a certain size. The doublet disappears from spectra below 200 K for the $CuFe_2O_4$ sample and below 100 K for the rest of the samples (x = 0.01, 0.02, 0.03). Moreover, the SR sextet vanishes from the $CuFe_2O_4$ spectra near 200 K, but it appears on the Mössbauer spectra of $CuFe_{2-x}Eu_xO_4$ (x = 0.01, 0.02, 0.03) over the whole temperature range. Therefore, the $CuFe_2O_4$ sample has the narrowest distribution of grain size nanoparticles.

The areas of $S_A$ and $S_B$ sextets of the $CuFe_2O_4$ Mossbauer spectra have equal values, suggesting that $Fe^{3+}$ ions equally occupy both A and B sites. The partial substitution of $Fe^{3+}$ ions by $Eu^{3+}$ ions results in higher values of the $S_A$ sextet area. The area value of $S_A$ sextet increases with the x growing. Thus, in the system $CuFe_{2-x}Eu_xO_4$, the $Eu^{3+}$ ions tend to occupy the octahedral B-site. The highest hyperfine magnetic field (H) values are observed for the $CuFe_2O_4$ Mössbauer spectrum. The introduction of $Eu^{3+}$ ions into the B-site leads to the reduction of H values. The decrease in H values of $S_A$ and $S_B$ sextets is probably caused by changes in the local structure resulting from cation substitutions. The partial substitution of $Fe^{3+}$ ions by $Eu^{3+}$ ions causes the redistribution of A and B cations, which leads to the alteration in angle and bond length of magnetic superexchange links.

### 3.4. Magnetic analysis

The M-H loop of $CuFe_{2-x}Eu_xO_4$ nanoparticles at ambient temperature as displayed in Fig. 7. Copper ferrite is a soft ferromagnetic material that has an inverse spinel structure with $Cu^{2+}$ ions at the A-site and $Fe^{3+}$ ions at both the A and B-sites [48]. The M-H curves of hysteresis loop is reveals the soft magnetic behavior and it shows saturated magnetization even at 20 kOe is characterized to the superparamagnetic behavior. The remanence (S) was quantified by utilizing relation $S = M_r/M_s$. The cubic anisotropy ($K_c$) was quantified by utilizing relation $K_c = \frac{H_c X M_s}{0.64}$. The uniaxial anisotropy ($K_u$) was quantified by utilizing relation $K_u = \frac{H_c X M_s}{0.985}$ [49,50]. Where, the saturation magnetization ($M_s$) and remanent magnetization ($M_r$) were recorded by using y- axis at M-H loop. Coercivity field (Hc) was quantified by the x- axis at M-H loop. The remanant magnetization (Mr), coercivity (Hc) and saturation magnetization (Ms),
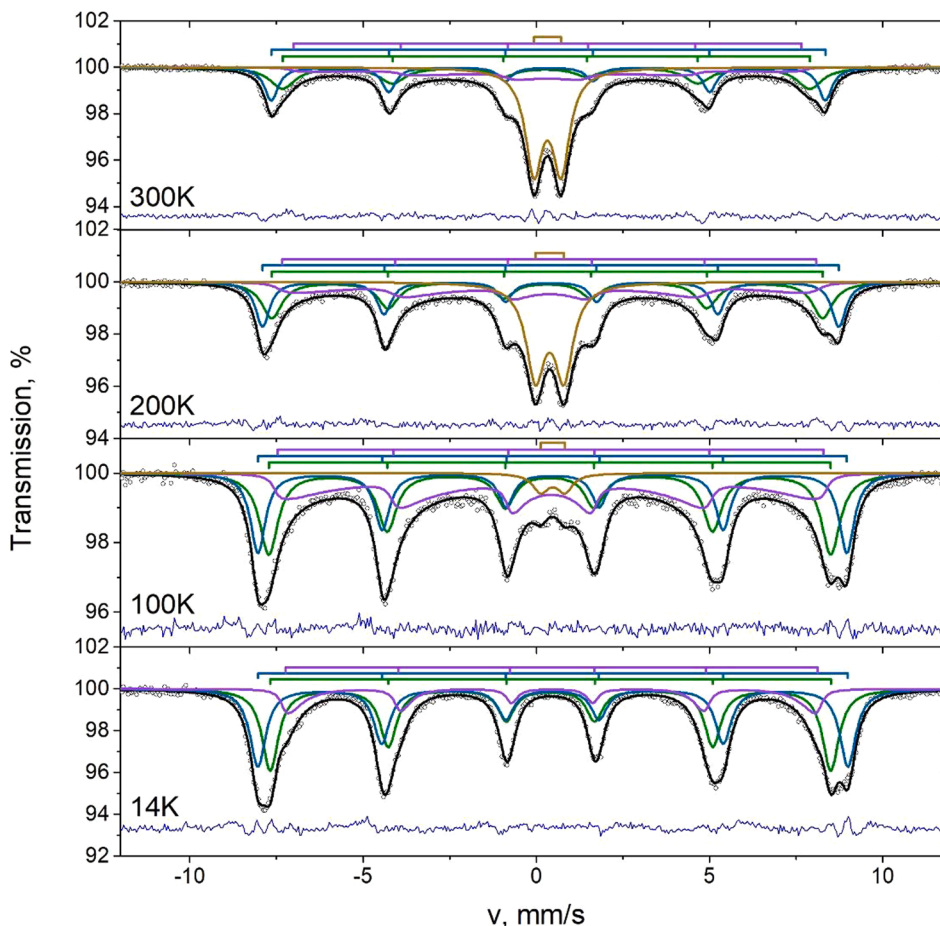
**Fig. 5.** Mössbauer spectra of $CuFe_{2-x}Eu_xO_4$ (x = 0.2) nanoparticles taken at different temperatures. (Greed line – $S_A$ sextet, Light blue line – $S_B$ sextet, Viol line – relaxation sestet, Dark yellow line – Doublet for unblocked particles).

remanence (S), uniaxial anisotropy ($K_u$) and cubic anisotropy ($K_c$) values for the $CuFe_{2-x}Eu_xO_4$ nanoparticles are tabulated in Table 3.

Magnetic parameters of the material depend on the crystallite size, crystal structure, shape, particle size, and interaction with the matrix. Fig. 7 clear that the $CuFe_{2-x}Eu_xO_4$ nanoparticles exhibit weak ferromagnetic behavior.

The increase of $Eu^{3+}$ concentration, the magnetization value gets varies may due to the varies in crystallite size as well [51]. As per nanosized materials, domain walls, the impurity phase ($\alpha$-$Fe_2O_3$) and small domain area are forestalling their revolution or spin which add to diminish the polarization [52]. Table clearly indicated that all magnetic parameters decrease sharply with x = 0.00 concentration to x = 0.01 concentration, the magnetic parameters increase sharply with x = 0.01 concentration to x = 0.02 concentration and again the magnetic parameters decreases with x = 0.02 concentration to x = 0.03 concentration. On the whole, the increasing $Eu^{3+}$ concentration more than appropriate ratio (1:2) significantly decreases the $M_s$ value of $CuFe_2O_4$ nanoparticles. The existence of impurity phases may cause in decreasing of magnetization [52,53]. Furthermore, at ambient temperature, the impurity phases are usually a canted antiferromagnetic phase with very weak magnetic behavior, reducing the total magnetic behavior of samples [52,53]. We discovered that the product's enhanced magnetic behavior is aided by its high crystalline nature, crystallite size, and very fine clear particle edges with minimal agglomeration morphology. Furthermore, the $Eu^{3+}$ concentration played an unavoidable role in the magnetic properties of $CuFe_2O_4$ nanoparticles.

Table 3 contains the remanent magnetization (Mr) values obtained from the M-H loop's intercept on the magnetization axis. It can be shown that the Mr values did not change monotonically with the samples' Eu

contents. The sample with x = 0.03 had the lowest Mr value, indicating that there may have been a minor doping of the Eu3 + ions, as the sample exhibits "greater" superparamagnetic-like behaviour. The particle-particle contact decreases as superparamagnetic behaviour increases..

Reduced remanence (S), which is the ratio between the Mr and Ms values of the respective samples, was taken into consideration to help us better comprehend this feature. As expected, the value of the lowered remanence was unexpectedly found to be lowest for the sample with x = 0.03 and to be higher for higher Sm-doping. However, the reduced remanence (S) of a collection of magnetic particles that are not in contact with one another is given by for samples with uniaxial anisotropy and by 0.832 for samples with cubic anisotropy by the Stoner-Wohlfarth model. The observed values of S in our samples are below 0.5 for samples with x = 0.03 but are high for those with lower concentrations (Table 3). This implies that samples have larger, non-interacting single domain particles that exhibit uniaxial anisotropy, while samples have smaller, mostly non-interacting single domain particles, and the type of anisotropy observed is cubic. It's noteworthy to observe that by doping more Eu3 + at the B-site, there is a transition from uniaxial anisotropy to cubic anisotropy. Additionally, there are two ways that the coercive field (Hc) in particulate systems might arise: I through inter-particle interactions, and (ii) through intra-particle interactions. Surface pinning and bulk magnetocrystalline anisotropy may both be responsible for the intra-particle interactions.

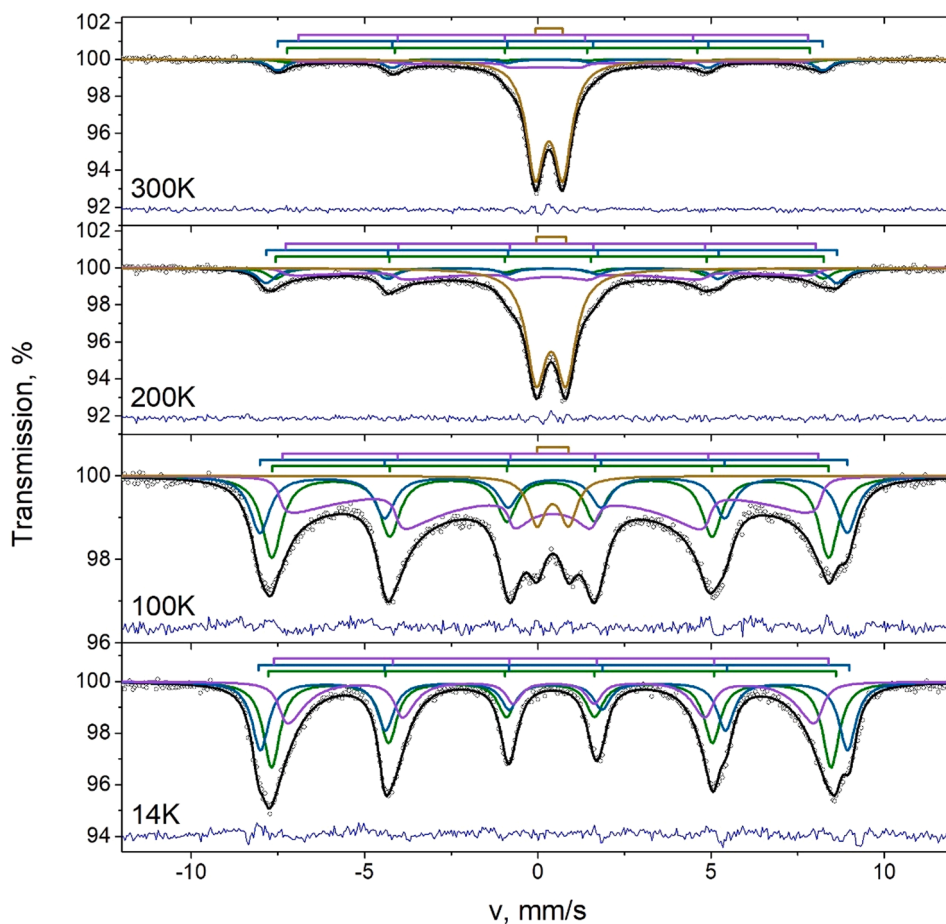All reported values is well matches with our results [1,2,3].

**Fig. 6.** Mössbauer spectra of $CuFe_{2-x}Eu_xO_4$ (x = 0.03) nanoparticles taken at different temperatures. (Greed line – $S_A$ sextet, Light blue line – $S_B$ sextet, Viol line – relaxation sestet, Dark yellow line – Doublet for unblocked particles).
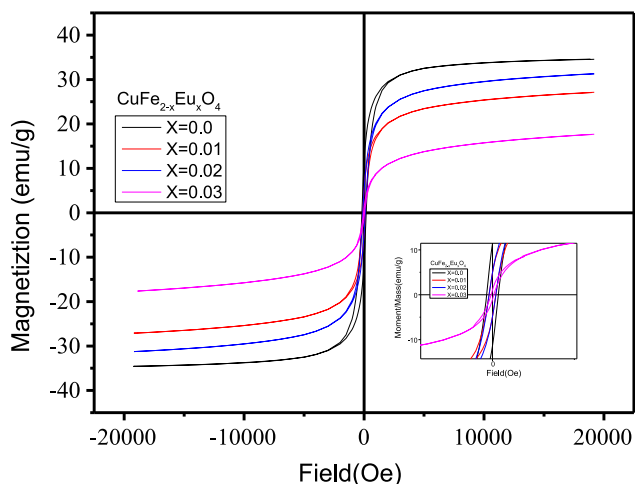


**Fig. 7.** The field dependent magnetization (*M-H*) curves at room temperature for $CuFe_{2-x}Eu_xO_4$ nanoparticles.

### 3.5. DFT calculations

In this section, the structural, energetics, and electronic structure of $CuFe_{2-x}Eu_xO_4$ was investigated based on DFT/PBE0 calculations. First, the optimized lattice parameters for pure $CuFe_2O_4$ were calculated as a = 8.403 Å, while the Eu-doped showed a = 8.473 and a = 8.476 Å for tetrahedral and octahedral doping sites, respectively, indicating a unit

**Table 3**
Magnetic parameters of $CuFe_{2-x}Eu_xO_4$ nanoparticles.

| $CuFe_{2-x}Eu_xO_4$ | Ms (emu/g) | Mr (emu/g) | Hc (Oe) | S | Ku (erg/Oe) | Kc (erg/Oe) |
|---|---|---|---|---|---|---|
| X = 0 | 33.374 | 10.779 | 188.08 | 0.322 | 6372.57 | 9807.78 |
| X = 0.01 | 22.961 | 4.688 | 98.746 | 0.169 | 2301.83 | 3542.66 |
| X = 0.02 | 27.712 | 4.890 | 103.448 | 0.202 | 2910.40 | 4479.29 |
| X = 0.03 | 14.342 | 0.922 | 42.319 | 0.064 | 616.18 | 948.34 |

cell expansion following the experimental analysis (Table 1). Therefore, the computed energies were analyzed to ascertain the preferential Eu-site doping, indicating that Eu-doping on the octahedral site is most favorable by 207.36 meV due to the largest $Eu^{3+}$ ionic radii in comparison to $Fe^{3+}$. However, it is important to mention that the calculated energy difference between tetrahedral and octahedral doping is relatively small, indicating that the Eu doping mechanism can occur at both sites, as predicted by Mossbauer's analysis.

As regards the magnetic properties of $CuFe_{2-x}Eu_xO_4$, the calculated energy values for FEM, FiM-I, and FiM-II models indicates that pure and Eu-doped systems are ferrimagnetic, once the Neel ferromagnetic configuration (FiM-I) is more stable by 416.28 (387.66) and 150.67 (132.23) meV in comparison to FEM and FiM-II configurations for pure (doped) $CuFe_2O_4$. Indeed, the calculated energy differences indicate that the Eu-doping mechanism induces a local structural disorder that affects the exchange-coupling constant between tetrahedral and octahedral sites.

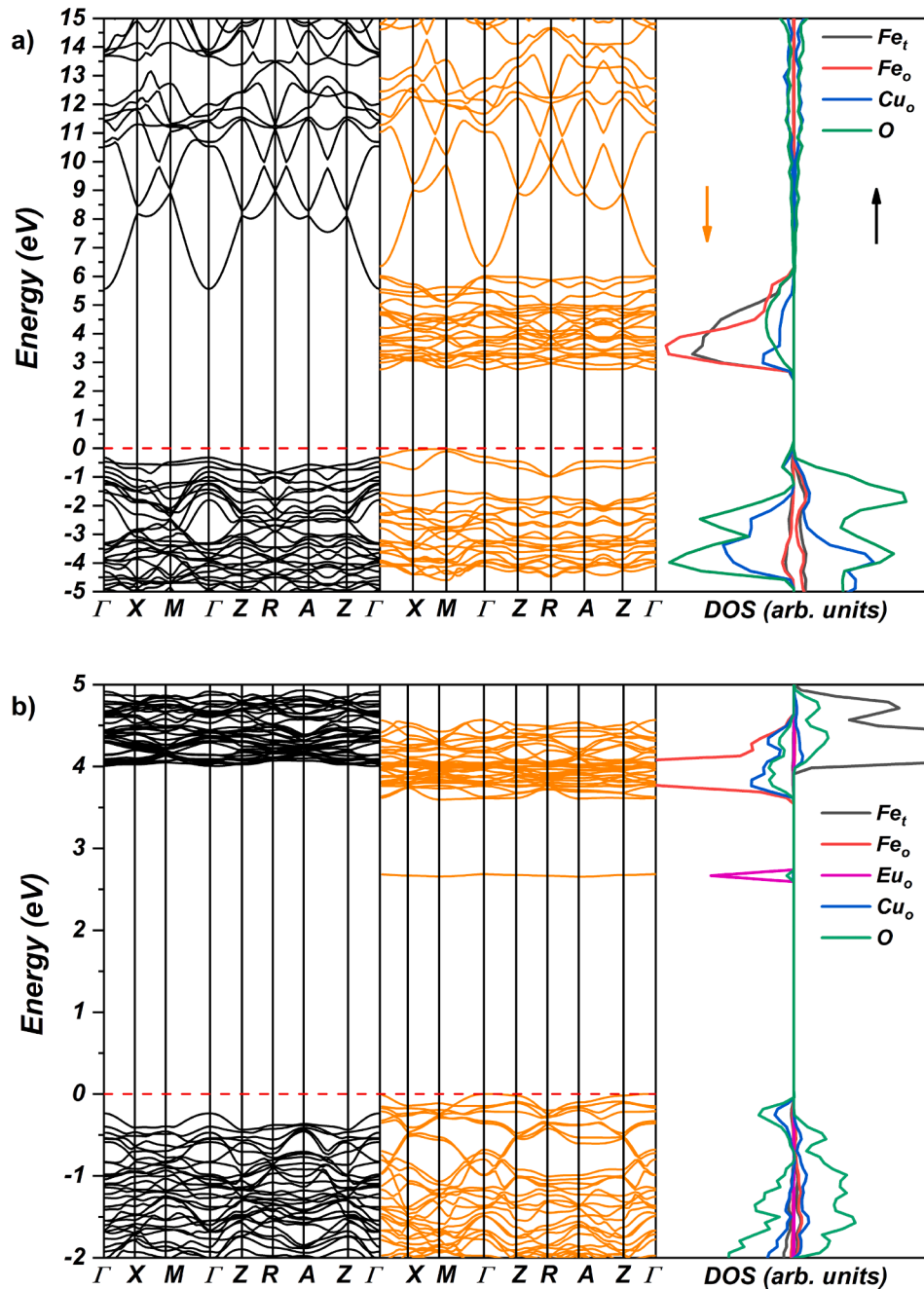In addition, it was observed that valence band maximum is flat along

**Fig. 8.** Band Structure and atom-resolved Density of States profiles for (a) pure and (b) Eu-doped $CuFe_2O_4$ models.

with M-Γ points, indicating that direct (M-M) and (Γ-M) band gaps are the same, which can affect the effective hole mass and trapping at the octahedral Cu (3d) orbitals located on this region. In particular, the electronic excitation can be described from $[CuO_6]$ to $[FeO_6]/[FeO_4]$ through the intermetallic connection Cu-O-Fe that occurs for both sublattices.

On the other hand, the VB and CB for the Eu-doped model (Fig. 8b) present a similar pattern of the energy level distributions compared to the pure one with the increase of impurity levels within the fundamental band gap associated with the Eu 4f orbitals. Herein, the electronic excitation involves $[CuO_6]$, $[EuO_6]$, and $[FeO_6]$, suggesting that after the Eu-doping, the octahedral environment was perturbed by local structural distortions that reduce the bandgap energy to 2.63 eV and allows an internal electron excitation. This fact agrees with the calculated energy differences between the magnetic models indicating that

intra-octahedral exchange-coupling constants were modified after the Eu-doping [54-61].

## 4. Conclusion

In the present work samples were prepared by using a self-propagating high temperature synthesis method, exhibiting a crystalline nature with a spinel cubic structure along with a small amount of impurity phase. The presence of functional groups of spinel ferrites was exhibited by FTIR spectra of the ferrites, confirming the cation distribution along with tetrahedral and octahedral voids. The temperature dependent Mössbauer spectra of $CuFe_{2-x}Eu_xO_4$ (x = 0, 0.01, 0.02, 0.03) (CEF) were collected at 300 K, 200 K, 100 K and 14 K. Room temperature spectra consist of asymmetrically broadened sextets and quadruple split lines. The intensity of quadrupole split lines decreases along with the

reduction of temperature. The observed changes in the structure of the Mössbauer spectra are typical of nanosized particles. The presence of paramagnetic lines at temperatures lower than the Curie temperature as well as asymmetric lines with sharp external fronts and significantly diffused internal fronts is the sign of superparamagnetic relaxation. The partial substitution of $Fe^{3+}$ ions by $Eu^{3+}$ ions causes the redistribution of A- and B- cations, which lead to the in alteration in angle and bond length of magnetic super exchange links. In particular, the Eu-doping mechanism is favored at octahedral site as proved by DFT calculations. Moreover, the rare-earth doping induces the bandgap narrowing due to the localization of intermediary energy levels associated with the 4f orbitals.

## CRediT authorship contribution statement

**V. Jagadeesha Angadi :** Conceptualization, Writing - original draft. **I.S. Yahia:** Formal analysis, Funding acquisition. **H.Y. Zahran:** Writing – review & editing. **M.C. Oliveira:** Data curation, Software. **E. Longo:** Writing – review & editing. **S.P. Kubrin:** Analysis of Mossbauer data. **S. O. Manjunatha:** Characterization. **R.A.P Ribeiro:** DFT calculation. **M. H. Ghozza:** Review.

## Declaration of Competing Interest

The authors declare that they have no known competing financial interests or personal relationships that could have appeared to influence the work reported in this paper.

## Data availability

Data will be made available on request.

## References

[1] E.-A. ThomasDippong, C.L. Lengauer, DanaToloman AndradaDaniel, O. Cadar, Mater. Charact. 163 (2020) 110268.

[2] T. Dippong, Erika Andrea Levei, Oana Cadar, Materials 14 (5) (2021) 1139.

[3] T. Dippong, Erika Andrea Levei, Oana Cadar, Iosif Grigore Deac, Mihaela Lazar Gheorghe Borodi, Ioan Petean, J. Alloy. Compd. 849 (2020) 156695.

[4] I. C. Sathisha, K. Manjunatha, A. Bajorek, B. Rajesh Babu, B. Chethan, T. Ranjeth Kumar Reddy, Y. T. Ravikiran and V. Jagadeesha Angadi, J. Alloys Compd. 848 (2020) 156577.

[5] B. Mondal, M. Kundu, S.P. Mandal, R. Saha, U.K. Roy, A. Roychowdhury, D. Das, ACS Omega 4 (2019) 13845–13852.

[6] P. N. Dayana, M. J. Abel, P. F. H. Inbaraj, S. Sivaranjani, R. Thiruneelakandan and J. J. prince, J. Cluster Sci. (2021). DOI: 10.1007/s10876-021-02094-5.

[7] R.S. Yadav, I. Kuřitka, J. Vilcakova, J. Havlica, J. Masilko, L. Kalina, J. Tkacz, M. Hajdúchová, V. Enev, J. Mater. Sci.: Mater. Electron. 28 (2017) 6245–6261.

[8] G. Raja, S. Gopinath, R.A. Raj, A.K. Shukla, M.S. Alhoshan, K. Sivakumar, Phys. E: Low-Dimens. Syst. Nanostruct. 83 (2016) 69–73.

[9] K. Elayakumar, A. Manikandan, A. Dinesh, K. Thanrasu, K. Kanmani Raja, R. Thilak Kumar, Y. Slimani, S.K. Jaganathan, A. Baykal, J. Magn. Magn. Mater. 478 (2019) 140–147.

[10] K. Elayakumar, A. Dinesh, A. Manikandan, M. Palanivelu, G. Kavitha, S. Prakash, R. Thilak Kumar, S.K. Jaganathan, A. Baykal, J. Magn. Magn. Mater. 476 (2019) 157–165.

[11] I. C. Sathisha, K. Manjunatha, V. J. Angadi, B. Chethan, Y. T. Ravikiran, K. P. Vinayaka, S. O. Manjunatha and M. Shidaling, in Mineralogy - Significance and Applications, ed. A. I. Al-Juboury, IntechOpen, 2020, DOI: 10.5772/intechopen.90880.

[12] I.C. Sathisha, K. Manjunatha, V.J. Angadi, R.K. Reddy, J. Supercond. Novel Magn. 33 (2020) 3963–3973.

[13] M.A. Almessiere, Y. Slimani, A.D. Korkmaz, A. Baykal, H. Güngüneş, H. Sözeri, S. E. Shirsath, S. Güner, S. Akhtar, A. Manikandan, RSC Adv. 9 (2019) 30671–30684.

[14] M.S. Shah, S. Aman, N. Ahmad, M.B. Tahir, Z.A. Alrowaili, M.S. Al-Buriahi, H.M. T. Farid, R.Y. Khosa, E.E. Hussein, A.Y. Elnaggar, Z.M. El-Bahy, J. Taibah Univ. Sci. 15 (2021) 798–804.

[15] M. N. Akhtar, M. Babar, S. Qamar, Z. u. Rehman and M. A. Khan, Ceram. Int. 45 (2019) 10187-10195.

[16] A. Kiran, M.N. Akhtar, M. Yousaf, K.M. Batoo, O.M. Aldossary, S.N. Khan, J. Rare Earths 39 (2021) 1224–1231.

[17] K. Manjunatha, I.C. Sathish, S.P. Kubrin, A.T. Kozakov, T.A. Lastovina, A. V. Nikolskii, K.M. Srinivasamurthy, M. Pasha, V.J. Angadi, J. Mater. Sci.: Mater. Electron. 30 (2019) 10162–10171.

[18] L.H.R, M. K, J. A. V, M. P. U and J. Husain, *Nano-Struct. Nano-Objects*, 2020, **24**, 100608.

[19] M.H. Abdellatif, G.M. El-Komy, A.A. Azab, J. Magn. Magn. Mater. 442 (2017) 445–452.

[20] P.P. Naik, R.B. Tangsali, S.S. Meena, S.M. Yusuf, Mater. Chem. Phys. 191 (2017) 215–224.

[21] R. Islam, M.A. Hakim, M.O. Rahman, H. Narayan Das, M.A. Mamun, J. Alloys Compd. 559 (2013) 174–180.

[22] A. Kumar, P.S. Rana, M.S. Yadav, R.P. Pant, Ceram. Int. 41 (2015) 1297–1302.

[23] P. Akhtar, M.N. Akhtar, M.A. Baqir, A. Ahmad, M.U. Khallidoon, M. Farhan, M. A. Khan, J. Mater. Sci.: Mater. Electron. 32 (2021) 7692–7703.

[24] J.F. Wang, C.B. Ponton, I.R. Harris, J. Magn. Magn. Mater. 298 (2006) 122–131.

[25] S. Amiri, H. Shokrollahi, J. Magn. Magn. Mater. 345 (2013) 18–23.

[26] K. M. Srinivasamurthy, K. Manjunatha, E. I. Sitalo, S. P. Kubrin, I. C. Sathish, S. Matteppanavar, B. Rudraswamy and V. Jagadeesha Angadi, Indian J. Phys., 2020, 94, 593-604.

[27] C. Adamo, V. Barone, J. Chem. Phys. 110 (1999) 6158–6170.

[28] R. Dovesi, A. Erba, R. Orlando, C.M. Zicovich-Wilson, B. Civalleri, L. Maschio, M. Rérat, S. Casassa, J. Baima, S. Salustro, B. Kirtman, Wiley Interdiscip. Rev.: Comput. Mol. Sci. 8 (2018) e1360.

[29] A.C. Ulpe, K.C.L. Bauerfeind, T. Bredow, ACS Omega 4 (2019) 4138–4146.

[30] K. Doll, N.M. Harrison, Chem. Phys. Lett. 317 (2000) 282–289.

[31] M. Catti, G. Valerio, R. Dovesi, Phys. Rev. B 51 (1995) 7441–7450.

[32] J.K. Desmarais, A. Erba, R. Dovesi, Theor. Chem. Acc. 137 (2018) 28.

[33] T. Bredow, K. Jug, R.A. Evarestov, Phys. Status Solidi B 243 (2006) R10–R12.

[34] H.J. Monkhorst, J.D. Pack, Phys. Rev. B 13 (1976) 5188–5192.

[35] N. Najmoddin, A. Beitollahi, M. Muhammed, N. Ansari, E. Devlin, S.M. Mohseni, H. Rezaie, D. Niarchos, J. Åkerman, M.S. Toprak, J. Alloys Compd. 598 (2014) 191–197.

[36] S. Pavithradevi, N. Suriyanarayanan, T. Boobalan, J. Magn. Magn. Mater. 426 (2017) 137–143.

[37] K. Manjunatha, V. Jagadeesha Angadi, K.M. Srinivasamurthy, S. Matteppanavar, V. K. Pattar, U. Mahaboob Pasha, J. Supercond. Novel Magn. 33 (2020) 1747–1757.

[38] K. Manjunatha, K. M. Srininivasamurthy, C. S. Naveen, Y. T. Ravikiran, E. I. Sitalo, S. P. Kubrin, S. Matteppanavar, N. Sivasankara Reddy and V. Jagadeesha Angadi, J. Mater. Sci.: Mater. Electron. 30 (2019) 17202-17217.

[39] C. Hou, D. Zhao, W. Chen, H. Li, S. Zhang, C. Liang, Nanomaterials 10 (2020) 426.

[40] A. Kumar, L. Rout, L.S.K. Achary, R.S. Dhaka, P. Dash, Sci. Rep. 7 (2017) 42975.

[41] N. Kazemi, M. Mahdavi Shahri, J. Inorg. Organomet. Polym. Mater. 27 (2017) 1264–1273.

[42] J.E. Tasca, A. Ponzinibbio, G. Diaz, R.D. Bravo, A. Lavat, M.G. González, Top. Catal. 53 (2010) 1087–1090.

[43] M.A. Chuev, Crystallogr. Rep. 65 (2020) 387–392.

[44] Y. V. Knyazev, D. A. Balaev, V. L. Kirillov, O. A. Bayukov and O. N. Mart'yanov, JETP Letters 108 (2018) 527-531.

[45] G.F. Goya, H.R. Rechenberg, Nanostruct. Mater. 10 (1998) 1001–1011.

[46] J.Z. Jiang, G.F. Goya, H.R. Rechenberg, J. Condens, Matter Phys. 11 (1999) 4063–4078.

[47] D.H. Jones, K.K.P. Srivastava, Phys. Rev. B 34 (1986) 7542–7548.

[48] V. Jagadeesha Angadi, K. Manjunatha, K. Praveena, V.K. Pattar, B. Jeevan Fernandes, S.O. Manjunatha, J. Husain, S.V. Angadi, L.D. Horakeri, K.P. Ramesh, J. Magn. Magn. Mater. 529 (2021) 167899.

[49] K. Manjunatha, V. Jagadeesha Angadi, R. Rajaramakrishna, U. Mahaboob Pasha, J. Supercond. Novel Magn. 33 (2020) 2861–2866.

[50] M. Abhishek, K. Manjunatha, V. Jagadeesha Angadi, E. Melagiriyappa, B. N. Anandaram, H.S. Jayanna, M. Veena, K.S. Acharya, C. Data, Collections 28 (2020) 100460.

[51] W. Ponhan, S. Maensiri, Solid State Sci. 11 (2009) 479–484.

[52] G. Litsardakis, I. Manolakis, K. Efthimiadis, J. Alloy. Compd. 427 (2007) 194–198.

[53] A.C.F.M. Costa, V.J. Silva, C.C. Xin, D.A. Vieira, D.R. Cornejo, R.H.G.A. Kiminami, J. Alloy. Compd. 495 (2010) 503–505.

[54] T. Dippong, E.A. Levei, L. Diamandescu, I. Bibicu, C. Leostean, G. Borodi, L. Barbu-Tudoran. Structural and magnetic properties of $Co_xFe_{3-x}O_4$ versus Co/Fe molar ratio//Journal of Magnetism and Magnetic Materials 394 (2015) 111–116. https://doi.org/10.1016/j.jmmm.2015.06.055.

[55] T. Dippong, O. Cadar, E. Andrea Levei, I.G. Deac, L. Diamandescu, L. Barbu-Tudoran, Influence of cobalt ferrite content on the structure and magnetic properties of $(CoFe_2O_4)_X$ $(SiO_2-PVA)_{100-X}$ nanocomposites//Ceramics, International 44 (2018) 7891–7901, https://doi.org/10.1016/j.ceramint.2018.01.226.

[56] M.A. Almessiere, Y. Slimani, A.V. Trukhanov, A. Baykale, H. Gungunes, E.L. Trukhanova, S.V. Trukhanov, V.G. Kostishin, Strong correlation between $Dy^{3+}$ concentration, structure, magnetic and microwave properties of the $[Ni_{0.5}Co_{0.5}]$ $(Dy_xFe_{2-x})O_4$ nanosized ferrites, J. Ind. Eng. Chem. 90 (2020) 251–259.

[57] S. Akhtar, S. Rehman, M.A. Almessiere, Firdos Alam Khan, Yassine Slimani, Abdulhadi Baykal, Nanomaterials 9 (11) (2019) 1635, https://doi.org/10.3390/nano9111635.

[58] Y. Slimani, B. Unal, M.A. Almessiere, A. Demir Korkmaz, S.E. Shirsath, A.V. Ghulam Yasin, A.B. Trukhanov, Results Phys. 17 (2020) 103061.

[59] M.A. Almessiere, Y. Slimani, M. Sertkol, F.A. Khan, M. Nawaz, H. Tombuloglu, E.A. Al-Suhaimi, A. Baykal, Ceramics International, 45 (2019) 16147-16156.

[60] Mircea Stefanescu, Marcela Stoia, Costica Caizer, Thomas Dippong, Paul Barvinschi, J. Therm. Anal. 97, Article number: 245 (2009).

[61] Thomas Dippong, Oana Cadar, Erika Andrea Levei, Iosif-Grigore Deac Gheorghe Borodi, Ceram. Int. 44 (9), 10478-10485.